CrossMark

Green Catalytic Degradation of Ethyl Acetate Incurred by Strong Interaction Between PdO and $Ce_{0.5}Co_{0.5}$ Support at Low Temperature

Sadia Akram[1,2] · Lan Chen[1] · Qi Wang[1] · Xiaorui Zhang[1,2] · Ning Han[3] · Genli Shen[1] ·
Zhen Wang[1] · Guanglu Ge[1]

Abstract Metal oxide-supported noble metal catalysts have been confirmed to be highly efficient and green in catalytic degradation of VOCs at low temperature and high concentration. Understanding the interaction between the noble metal and various oxide supports is crucial in improving catalytic performance. Herein, lattice doped Ce-Co composite oxide ($Ce_{0.5}Co_{0.5}$) has been used to support PdO species for the decomposition of ethyl acetate (EA). The catalytic activity of the supported PdO catalyst at a feed rate $R_{140}\,°C = 1.38 \times 10^{-4}$ mol g_{cat}^{-1} s^{-1} was enhanced compared with that of the support at a feed rate $R_{140}\,°C = 0.7$ 5×10^{-4} mol g_{cat}^{-1} s^{-1}. The enhanced catalytic activity of the Ce/Co-supported noble metal catalyst ($PdO/Ce_{0.5}Co_{0.5}$) is attributed to the strong metal-support interaction (SMSI). The effect of PdO addition and its interaction with the support has been investigated by a set of comprehensive characterization technologies on an elaborately-designed model catalytic system. In addition, in-situ DRIFT analysis shows that no harmful intermediate product, such as aldehydes other than alcohols and acetate is produced during the reaction, suggesting this promising green approach.

Sadia Akram and Lan Chen have contributed equally.

Electronic supplementary material The online version of this article (doi:10.1007/s10562-016-1906-3) contains supplementary material, which is available to authorized users.

✉ Zhen Wang
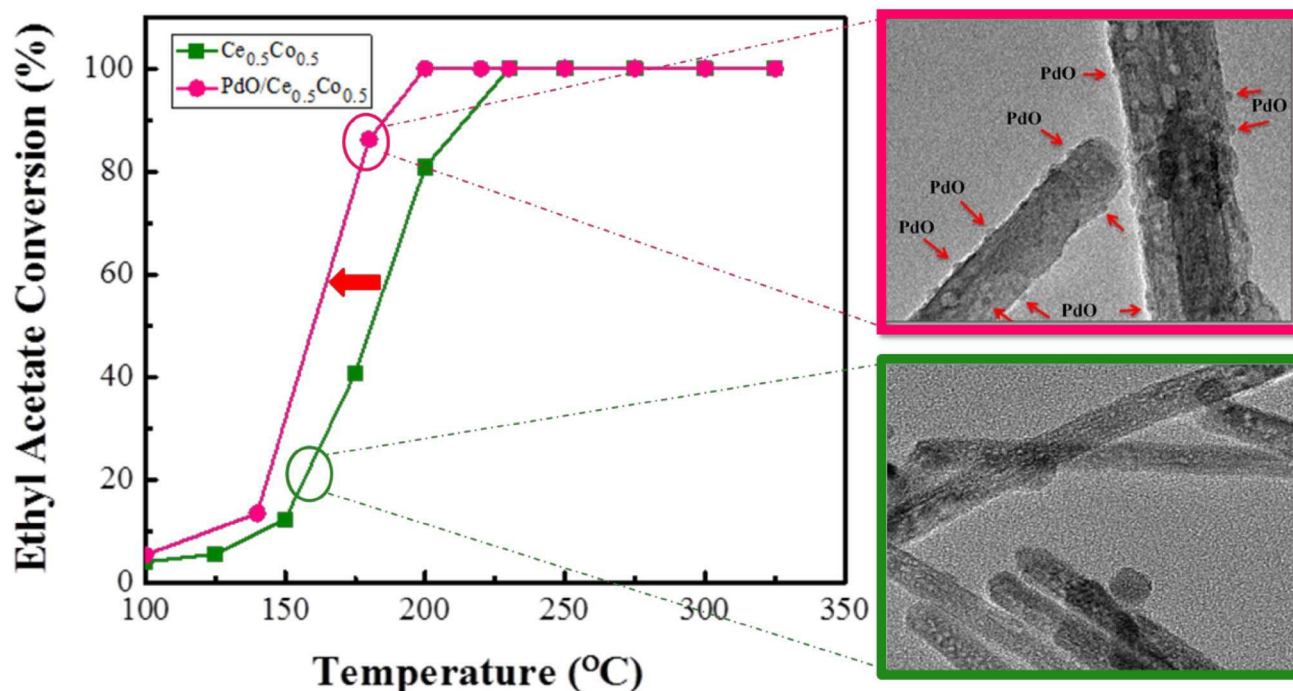 wangzh@nanoctr.cn

✉ Guanglu Ge
 gegl@nanoctr.cn

1   CAS Key Laboratory of Standardization and Measurement
   for Nanotechnology, and CAS Centre for Excellence
   in Nanoscience, National Centre for Nanoscience
   and Technology, No.11 Zhongguancun Beiyitiao,
   Beijing 100190, China

2   University of Chinese Academy of Science, No. 19 A
   Yuquan Road, Beijing 100049, China

3   State Key Laboratory of Multiphase Complex Systems,
   Institute of Process Engineering, Chinese Academy
   of Sciences, Beijing 100190, China

Graphical Abstract

1 Introduction

Over the past decade, the emission of volatile organic compounds (VOCs) has become a hot topic as they are the major contributors to the production of photochemical smog and ground level ozone. They are emitted from numerous industrial and anthropogenic sources and are hazardous to human health as they are mutagenic and carcinogenic. Thus, to relate the VOCs emission and exposure with mortality and morbidity is reasonable. These health and environmental issues have led numerous countries to regulate the policies aimed at the reduction and emanation of VOCs [1–6].

To date, a substantial amount of research work has been done to develop technologies for the efficient removal of VOCs. Among these technologies, catalytic oxidation is very promising to meet the requirements such as high competency at low temperature, eco-friendliness, low cost, energetically affordability along with negligible production of SO_x and NO_x [7].

$VIII_B$ noble metals such as palladium and platinum containing catalysts are very useful and indispensible to achieve higher catalytic activities at lower temperature owing to their enhanced resistance to thermal deactivation, excellent catalytic activity and facile catalyst regeneration [8–10]. However, these precious metals are expensive due to the limited reserves. Thus, the fabrication of the catalyst with least amount of noble metal is of importance for effective use of the precious species. The noble metal decorated catalysts is one of widely-used approaches to achieve this goal, where the noble metal species are well-dispersed and spread over oxide substrates forming active component by the minimum usage of Pd or Pt along with the enhanced stability and improved performances [11, 12]. In addition, the interaction between noble metal and its support named "strong metal-support interaction" (SMSI) significantly affects the catalytic properties of the system and can be tuned by the chemical nature of support and the extent of the noble metal dispersion. Thus the excise control to the interaction between the interface of the noble metal particles and the support is a pivot factor to improve the catalytic activity and catalyst life [13, 14].

In this regard, ceria is the most popular rare earth oxide widely used as a support alone or by hybridizing with other metal oxides, because of its unique redox performance and remarkable oxygen storage/mobility properties [15–22]. However, the detailed understanding of the reaction mechanism and the interaction between the noble metal and its support remains elusive due to complex nature of these catalytic systems.

Recently [21] our group has investigated a series of lattice doped CeO_2-Co_3O_4 nanocomposites for the oxidative removal of EA and determined the interaction between

the components of composite oxide that affects the catalytic activity. In this work, the main focus is to explore the effect of PdO addition to the system and its interaction with support ($Ce_{0.5}Co_{0.5}$) as well as its impacts on VOCs oxidation performance at significantly reduced temperature under a concentrated feed stream. In order to evaluate the effect of PdO addition, the physiochemical properties and the catalytic performance for both support and noble metal deposited catalyst, XRD, XPS, Raman and TPR analysis have been used to systematically investigate the interaction between $Ce_{0.5}Co_{0.5}$ and the PdO. Furthermore, detailed investigation on the degradation mechanism of EA by time resolved in-situ DRIFT analysis has been done. It is anticipated that the model catalytic system described here would be generally applicable in the development of other similar catalysts for the complete catalytic degradation of EA or similar organic compounds by a greener approach at reduced temperature without the formation of other harmful intermediates other than alcohols and acetates.

2 Experimental

2.1 Catalyst Preparation

A facile surfactant-free hydrothermal method is used to prepare the support materials ($Ce_{0.5}Co_{0.5}$) synthesized from the nitrates of cerium and cobalt in accordance with the procedure described previously [21]. In a typical preparation, an aqueous solution of concentrated NaOH (6M) was mixed with a aqueous solution of $Ce(NO_3)_3 \cdot 6H_2O$ (Sinopharm chemical reagents, 99%) and $Co(NO_3)_2 \, 6H_2O$ (Tianjin Fuchen chemical reagents, 99%) in appropriate amount. The resulting solution was poured into a Teflon lined autoclave, heated and kept at 120 °C for 24 h in an oven. The resultant precipitates were washed with distilled water and ethanol sequentially for several times and collected by centrifugation. The obtained product was dried at 80 °C and calcinated at 550 °C for more than 2 h. $PdO/Ce_{0.5}Co_{0.5}$ was synthesized with a modified multi-step method [23]. Firstly, the as-synthesized $Ce_{0.5}Co_{0.5}$ was mixed with Na_2PdCl_4 solution (0.01 M, 10 mL) at room temperature and an appropriate amount of $Na_3C_6H_5O_7 \cdot 2H_2O$ was added as the reducing agent into the mixture after it rises to 60 °C. The reaction mixture was processed at the temperature for 5 h. Finally, the precipitates were harvested, dried under vacuum at 80 °C for 24 h and calcined under ambient atmosphere at 550 °C for 2 h.

2.2 Characterization

Surface composition was determined by X-ray photoelectron spectroscopy (XPS) using an ESCALab220i-XL electron spectrometer from VG Scientific with a monochromatic Al Kα radiation. The binding energy (BE) was referenced to the C1s line at 284.8 eV from adventitious carbon.

The textural characterization was obtained from the adsorption isotherms of N_2 at 77 K using an Autosorb-1 analyzer (Quantachrome). Before measurement, the samples were degassed at 573 K for 4 h under vacuum. The crystal structure of the materials was examined by X-ray diffraction (XRD, Philips X'pert PRO) equipped with a Cu Kα radiation source ($\lambda_e = 0.154187$ nm) at a scanning rate of $0.03° \, s^{-1}$ (2θ from 10° to 90°). The selected samples were also analyzed by Inductively Coupled Plasma-Mass Spectrometry (ICP-MS) to determine the content of Ce, Co and Pd in each sample. Raman study was carried out by InVo- RENISHAW system at room temperature using a 514.5 nm laser.

Morphological and compositional characterization was carried out by high resolution transmission electron microscopy (HRTEM) (Tecnai G^2 F20 U-TWIN) with an accelerating voltage of 200 kV.

TPD measurements were carried out using NH_3 and CO_2 as probe molecules for acidity and basicity analysis, respectively. The operations were performed with a U-type quartz reactor equipped with Automated Catalyst Characterization System (Autochem 2920, MICROMERITICS). A typical experiment used a 100 mg sample (40–60 mesh) and a gas flow rate of 20 mL/min. The catalysts were firstly degassed under He flow at 823 K for 1 h. Subsequently, the sample was allowed to cool to 313 K under He flow. NH_3-He or CO_2-He was passed over the catalyst for 1 h at a rate of 10 mL/min to ensure complete adsorption. For desorption, the NH_3 or CO_2 saturated catalyst was then ramped from 313 K to 823 K at a heating rate of 10 K/min with He as the carrier to cause desorption. This amount desorbed at various temperatures is an indicator of the catalyst acidity or basicity respectively, and is expressed as millimole of absorbent per gram adsorbate.

To acquire the information of the sample reducibility, hydrogen temperature-programmed reduction (H_2-TPR) was conducted in a U-type quartz reactor equipped with Automated Catalyst Characterization System (Autochem 2920, MICROMERITICS). 50 mg of each sample (40–60 mesh) used for the analysis was loaded and pre-treated with an air flow mixed by 5% O_2 and 95% He (50 mL min^{-1}) at 423 K for 1 h and cooled to 323 K under a helium flow. The samples were then re-heated to 1173 K at a rate of 10 K min^{-1} under a flow consisting of 10% H_2 and 90% Ar (50 mL min^{-1}) to obtained TPR signals.

In-situ diffuse reflectance infrared Fourier transform spectroscopy (DRIFTS) were carried out on a Nicolet 6700 FTIR fitted with a liquid nitrogen-cooled mercury–cadmium–telluride detector (MCT). The DRIFTS cell

(Harrick, HVC-DRP) fitted with CaF_2 windows was used as the reaction chamber where the samples are allowed to be heated to 600 °C. The spectra of 50 mg of samples were recorded with the reaction progressed from RT to 400 °C under comparable conditions. All the spectra were collected within the range of 4000–1200 cm^{-1} at a resolution of 4 cm^{-1} and 64 scans per test. The composition of the feed stream is same to that of the catalytic reaction.

2.3 Catalytic Tests

The as-prepared support and Ce-Co-supported PdO catalysts have been evaluated for the oxidation of EA. The catalytic reactions were performed in a continuous-flow fixed-bed reactor containing 100 mg of catalyst samples (40–60 mesh) under ambient pressure. A standard reaction gas i.e. 1500 ppm of EA in a mixture of 25% O_2 and 75% N_2 was continuously fed at the rate of 100 mL min^{-1}. The weight hourly space velocity (WHSV) is typically 60,000 mL g^{-1} h^{-1}. On-line analysis on the products was done by GC/MS (Hewlett–Packard 6890N gas chromatograph interfaced to a Hewlett–Packard 5973N mass selective detector) with a HP-5MS capillary column (30 m × 0.25 mm × 0.25 µm). The catalytic activity is determined by the conversion of EA into CO_2 as shown below:

$$X_{ethylacetate} = \frac{C_{ethylacetate(in)} - C_{ethylacetate(out)}}{C_{ethylacetate(in)}} \times 100\%$$

3 Results and Discussion

3.1 Physiochemical Characterization of the Catalysts

Wide-angle XRD patterns of the as-prepared catalysts are shown in Fig. 1a. The peaks at $2\theta = 28.5°$, 33.1°, 47.5°, 56.4°, 69.4°, and 76.8° in pure CeO_2 are well-resolved and assigned to the typical fluorite cubic CeO_2 (JCPDS # 81-0792). In the case of pure Co_3O_4, all the diffraction peaks at $2\theta = 31.3°$, 36.9°, 44.8°, 59.4° and 65.4° match well with the spinal structure of Co_3O_4 (JCPDS # 74-2120). As seen in Fig. 1a, the pure compound shows better crystallinity than their composite counterparts. No crystalline peaks of the isolated PdO or spurious phases are observed in PdO/Ce$_{0.5}$Co$_{0.5}$ suggesting Pd clusters is too small to be identified by XRD and well-dispersed over the whole catalyst. Figure 1b reveals that the diffraction peak ($2\theta = 28.6°$) of the support materials (Ce$_{0.5}$Co$_{0.5}$) shifts to higher 2θ value with the increase of the dopant in pure CeO_2 phase, which implies the insertion of cobalt atoms into ceria lattice to form Ce–Co–O solid solution resulted in a contraction of the lattice parameters from 0.54 to 0.537 nm for CeO_2 phase [24]. Since the effective ionic radius of Co^{3+}

(0.065 nm) or Co^{2+} (0.082 nm) is smaller than that of Ce^{4+} (0.111 nm), these ions can easily replace Ce^{4+} and enter into CeO_2 lattice [25, 26]. Lattice microstrain is, therefore produced by such replacement, which is evaluated by XRD analysis and is given in supporting information (SI) (Fig. S1). The value for pure CeO_2 ($\varepsilon = 0.550$) is found to be lower than that of Ce$_{0.5}$Co$_{0.5}$ ($\varepsilon = 0.759$), which again confirms the insertion of cobalt ions into ceria lattice resulting in the increase of the strain-related defects, i.e. oxygen vacancy and oxygen mobility compared with pure CeO_2. However, the lattice strain is somehow relaxed ($\varepsilon = 0.668$) when Pd species are dispersed on the surface of this composite, indicating that a strong interaction exists between the active metal and support [27]. The enhanced catalytic activity of PdO/Ce$_{0.5}$Co$_{0.5}$ is considered to be imfluenced by this factor and further discussion will be seen in the following paragraphs.

For the detailed investigation on morphological characters, crystal structure and dispersion of active metal over the support, TEM and HRTEM and HAADF mapping were conducted (Fig. 2). A typical TEM image (Fig. S2) demonstrate the rod-like shape of the support with a length of 150–200 nm and diameter of 20–30 nm. In case of PdO/Ce$_{0.5}$Co$_{0.5}$ (Fig. 2a), it can be seen that the addition of PdO species did not alter the shape and size of the support materials which remains as nanorods, while the shape of PdO is spherical particles with a size of 2–5 nm marked by the red arrows. As identified by HRTEM, the crystal fringes can be assigned to (220) crystal plane of Pd species (PdO) and (111) crystal plane of the ceria (Fig. 2b). A careful EDX analysis of PdO/Ce$_{0.5}$Co$_{0.5}$ (Fig. S3) concludes that the catalyst is indeed composed of no elements other than Ce, Co, Pd and O. The minor peak of Cu is from the Cu TEM grids. In addition, the homogeneous dispersion of both the noble metal and support throughout the whole PdO/Ce$_{0.5}$Co$_{0.5}$ catalyst is observed by HAADF mapping (Fig. 2c), which is crucial to cause the interaction between support and active metal [28].

Thermogravimetric analysis (TGA) profiles of PdO/Ce$_{0.5}$Co$_{0.5}$ (Fig. S4) shows almost no weight loss up to 600 °C, attributed to the highly stable nature of the catalyst without elemental loss including Pd species except for negligible amount of the adsorbed water molecules. The BET surface area of PdO/Ce$_{0.5}$Co$_{0.5}$ is almost similar to that of Ce$_{0.5}$Co$_{0.5}$ (Table 1). Furthermore the pore volume of PdO/Ce$_{0.5}$Co$_{0.5}$ decreases slightly indicating that the Pd species are not fully incorporated into the pores of the support (Table 1) and prevent the destruction of the stacking pores. The composition of the catalyst was determined by ICP-MS (Table 1). The content of Ce and Co is 41.8 and 16.2 wt% respectively in the compound while oxygen account for the remaining 42 wt%. Pd content is 2.8% for the PdO/Ce$_{0.5}$Co$_{0.5}$ catalyst as analyzed by ICP-MS.

Fig. 1 XRD (**a**) wide-angle patterns, and (**b**) Enlarged-zone patterns. Crystalline phases detected CeO_2 (*asterisk*), Co_3O_4 (*filled circle*)
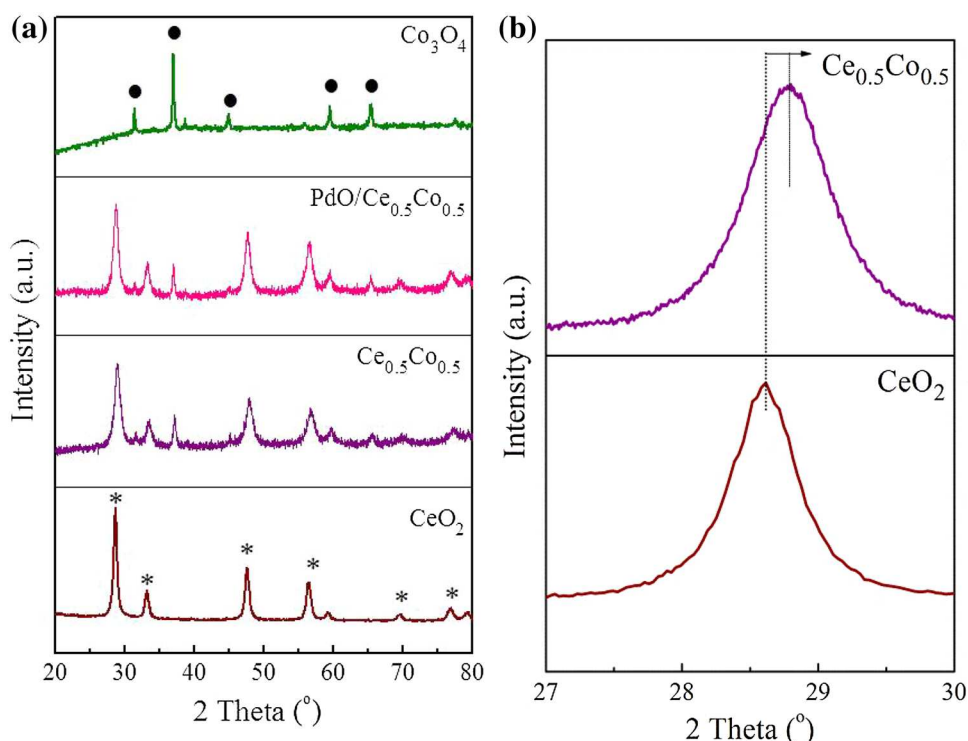
XPS not only provides the information about the surface composition and electronic state of the catalyst but also is a powerful tool to study the interaction between the support and active metal component. Figure 3a illustrates the XPS spectra of Ce 3d. The peaks are fitted by Gaussian-Lorenz model and the obtained 6 main features (V_0, V_0', V_1, V_1', V_2, V_2') can be ascribed to Ce^{4+} 3d final states [29, 30]. The high binding energy (BE) doublet (V_2/V_2' and V1/V1′) is attributed to the final state of $Ce(IV)3d^94f^0O2p^6$ and $Ce(IV)3d^94f^1O2p^5$ respectively, while the V_0/V_0' doublet corresponds to the state of $Ce(IV)3d^94f^2O2p^4$. Therefore, the dominant oxidation state of Ce species in the support is tetravalent [31]. The characteristic peaks of Ce^{3+} are also observed and labeled as U_1/U_1' and U_0/U_0', whereas the relative amount of Ce^{3+} is calculated to be 23% (SI: Eq. 1) based on the integrated peak areas for both Ce^{3+} and Ce^{4+}. A previous report has described the correlation between Ce^{3+} and the formation of oxygen vacancies in the catalyst, which play a vital role in the storage and mobility of oxygen during catalysis [32]. As seen from the above XPS results, it is clear that the support solid solution consists of both Ce^{4+} and Ce^{3+} species where the amount of Ce^{4+} is dominant.

As seen in Fig. 3b, Co 2p spectra present two main peaks at higher (794.4 eV) and lower (779.2 eV) BE attributed to Co $2p_{1/2}$ and Co $2p_{3/2}$, respectively. Due to small difference in the BE of Co^{2+} and Co^{3+}, they are not easily distinguished. It is well known that ΔE value (Co 2p peaks) for CoO, Co_2O_3, and Co_3O_4 is 16.0, 15.0 and 15.2 eV respectively [33, 34]. The examined ΔE value in Co 2p spectra is 15.2 eV so Co_3O_4 is considered as the main phase of cobalt in support which is consistent with XRD analysis.

The spectrum of $Ce_{0.5}Co_{0.5}$ in Fig. 3c shows a peak with a broad shoulder attributed to the overlapping of different oxygen species (O1s), which can be deconvoluted into three peaks at low, medium and high BEs respectively. The peak at low BE (529.0 eV) is attributed to lattice oxygen atoms (O^{2-}, denoted as O_α). The peak at medium BE (531.0 eV) is denoted as O_β indicate the surface adsorbed oxygen species (O^{2-}, O^- or O_2^{2-}) while a broad shoulder at higher BE (533.5 eV, denoted as O_γ) refers to the presence of the defective oxides, hydroxylated or carbonated oxygen on the surface of the catalysts [35]. The relative concentration of the lattice oxygen species in terms of O_α vs O_β for the pure CeO_2, Co_3O_4 and composite oxide support ($Ce_{0.5}Co_{0.5}$) is calculated in our previous work, which confirms that $Ce_{0.5}Co_{0.5}$ possesses the highest ratio of O_α/O_β. This again approves that the enhanced lattice oxygen storage and mobility is caused by CeO_2–Co_3O_4 interaction [36].

Figure 3d shows two distinct peaks at 337.2 and 342.6 eV assigned to Pd$3d_{5/2}$ and Pd$3d_{3/2}$ respectively. BE for Pd$3d_{5/2}$ with different valence has slight variation where the peaks at 337.7–338.4 eV, 336.7–336.9 eV and 335.0–335.4 eV are attributed to Pd^{4+}, Pd^{2+} and Pd^0, respectively. According to the previous report, the Pd^{2+} (PdO) $3d_{5/2}$ and $3d_{3/2}$ BE values are around ~337.0 and ~342.0 eV [37], close to one of the XPS profile lines at

**Fig. 2** TEM (**a**), HRTEM (**b**) images and STEM HAADF mapping (**c**) of PdO/Ce$_{0.5}$Co$_{0.5}$
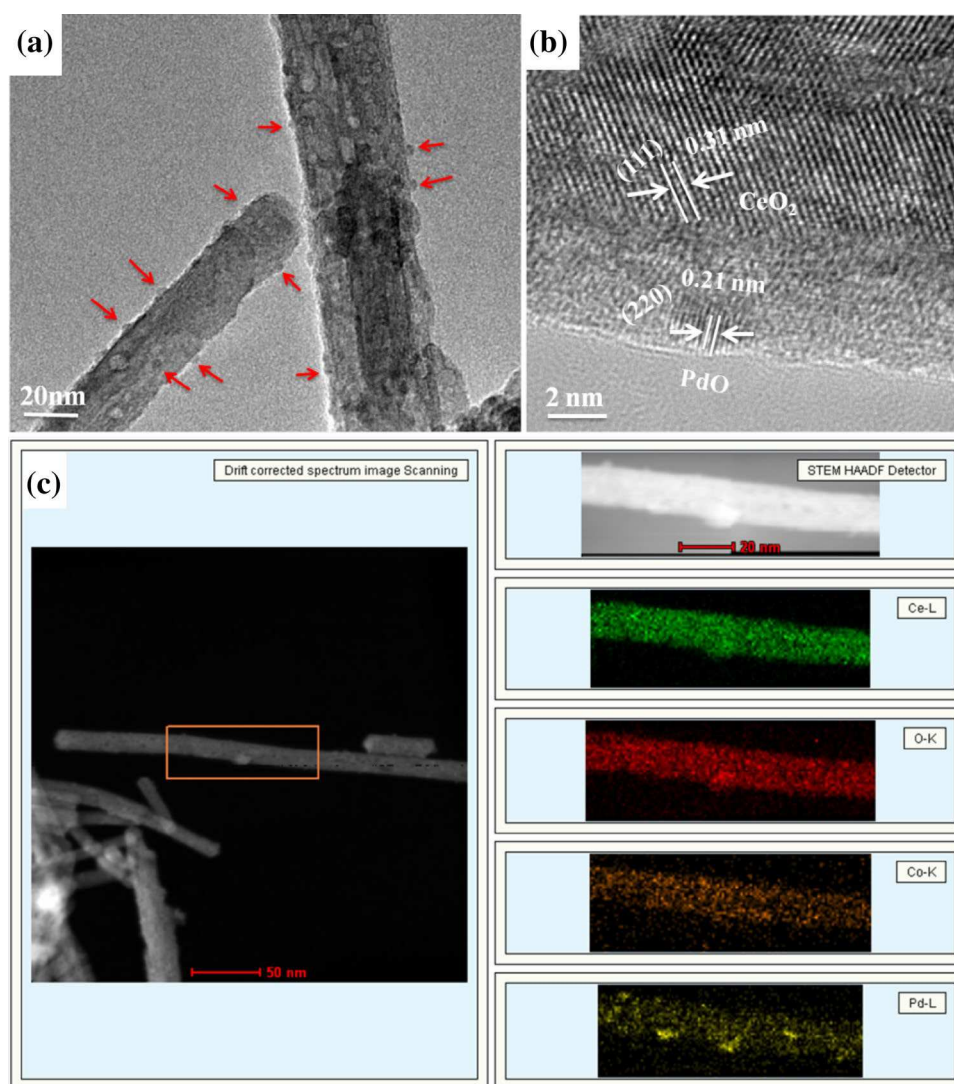
Table 1 Structural and compositional properties of the catalysts Ce$_{0.5}$Co$_{0.5}$ and PdO/Ce$_{0.5}$Co$_{0.5}$

Samples	BET area (m^2/g)	Pore volume (cm^3/g)	ICP analysis Conc. of elemental species (%)			
			Ce	Co	O	Pd
Ce$_{0.5}$Co$_{0.5}$	73	0.24	41.8	16.2	42	–
PdO/Ce$_{0.5}$Co$_{0.5}$	75	0.19	40.6	15.7	40.9	2.8

337.3 eV confirming that majority of the surface Pd species are in the form of PdO. This is in accordance to the fact that the surface Pd species are more electron deficient than bulk PdO. In short, this phenomenon can be attributed to the SMSI in the form of Pd-O-CeO$_{2-x}$ [37, 38]. Therefore, the Pd-O species are reasonably thought to exist in the form of Pd-O-support rather than Pd-O-Pd. Higher chemical shift in the BEs of Pd3d$_{5/2}$ and Pd3d$_{3/2}$ as shown in Fig. 3d again confirms the strong interaction between the support and PdO species [12, 39]. This finding is in a good agreement with HRTEM images and HAADF mapping, where

the well-dispersed PdO nanoparticles on the surface of the support are observed and this dispersion results from the interaction between the support and PdO. In addition, a comparison of Ce 3d, Co 2p and O1s has been given in SI (Table S2 and Fig S9) for Ce$_{0.5}$Co$_{0.5}$ and PdO/ Ce$_{0.5}$Co$_{0.5}$ catalysts. The XPS patterns (Fig S9) shows that the addition of the PdO nanoparticles in the catalytic system did not affect the oxidation state of the support.

Figure 4a reveals the Raman spectra for all the catalysts. Pure Co$_3$O$_4$ exhibits four Raman bands at 462 (E$_g$), 505 (F$_{2g}$), 597 (F$_{2g}$) and 670 cm^{-1} (A$_{1g}$) corresponding to E$_g$,
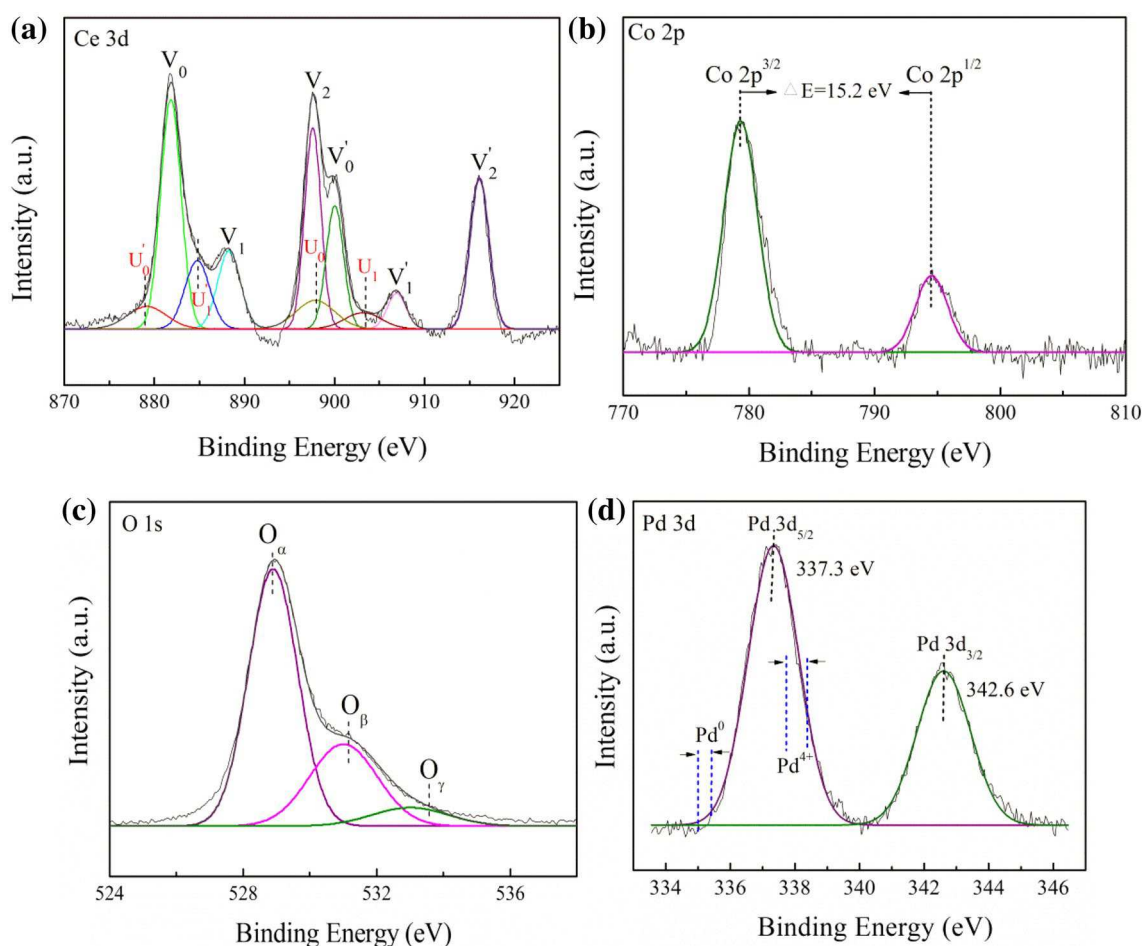
Fig. 3 X-ray photoelectron spectra for Ce 3d (**a**), Co 2p (**b**), O 1 s (**c**) of $Ce_{0.5}Co_{0.5}$ and Pd 3d (**d**) of $PdO/Ce_{0.5}Co_{0.5}$ catalyst

F_{2g} and A_{1g} vibration modes, respectively, consistent with the previous results [40, 41] which are identified as a spinel structure of Co_3O_4 by XRD. In the case of pure CeO_2, four bands appear at 265, 460 and 592, 1174 cm^{-1} are attributed to doubly degenerated TO mode, the triply degenerated Raman-active mode and the non-degenerated LO mode respectively. The most intense vibration at 460 cm^{-1} corresponds to the Raman active vibration mode (F_{2g}) of a cubic fluorite structure and represents the symmetric breathing mode of oxygen atom around cerium ions [42]. In the case of $Ce_{0.5}Co_{0.5}$, the central location of the strong band shifts towards a lower value from 460 cm^{-1} (Fig. 4b), which could be attributed to the formation of solid solution and the change in lattice parameters as a result of lattice doping of CeO_2 by Co atoms with the formation of oxygen vacancies [21]. In addition, a small hump occurs at around 670 cm^{-1} (Fig. 4a) which can be attributed to the existence of a separated Co_3O_4 phase. These findings are in accordance with XRD data. The broad shoulder around 590 cm^{-1} indicates a defect-induced mode, which is used to determine the content of the oxygen vacancy-related

defects caused by Ce^{3+} ions and oxygen in the support [25, 43]. The oxygen vacancies are beneficial for the adsorption of surface oxygen species and consequently favor the oxidation reaction [44]. These findings are consistent with the above XPS results. Raman spectrum of $PdO/Ce_{0.5}Co_{0.5}$ catalyst is similar to that of the supporting compounds and no distingushable PdO peaks appear in either Raman or XRD due to its small size. And the A_{1g} (Co_3O_4) peak at 670 cm^{-1} is significantly enhanced by depositing Pd. The reason for such enhancement will be further investigated in future. The ratio of the integrated peak area at 590 cm^{-1} (oxygen vacancy) and 460 cm^{-1} (main peak) is denoted as A_{OV}/A_{MP} which is an indicator for the relative amount of the oxygen vacancies. The concentration of oxygen vacancies in $PdO/Ce_{0.5}Co_{0.5}$ (0.7) is relatively higher than that of the support (0.6), which supports the strong interaction between $Ce_{0.5}Co_{0.5}$ and PdO.

The H_2-TPR profiles of $PdO/Ce_{0.5}Co_{0.5}$ and $Ce_{0.5}Co_{0.5}$ are displayed in Fig. 5. The reducibility of the individual pure oxides, CeO_2 and Co_3O_4 is also investigated as shown in Fig. S5. $Ce_{0.5}Co_{0.5}$ exhibits mainly three reduction peaks

Fig. 4 Raman spectra of the model catalysts, (**a**) wide angle patterns and (**b**) enlarged zone patterns
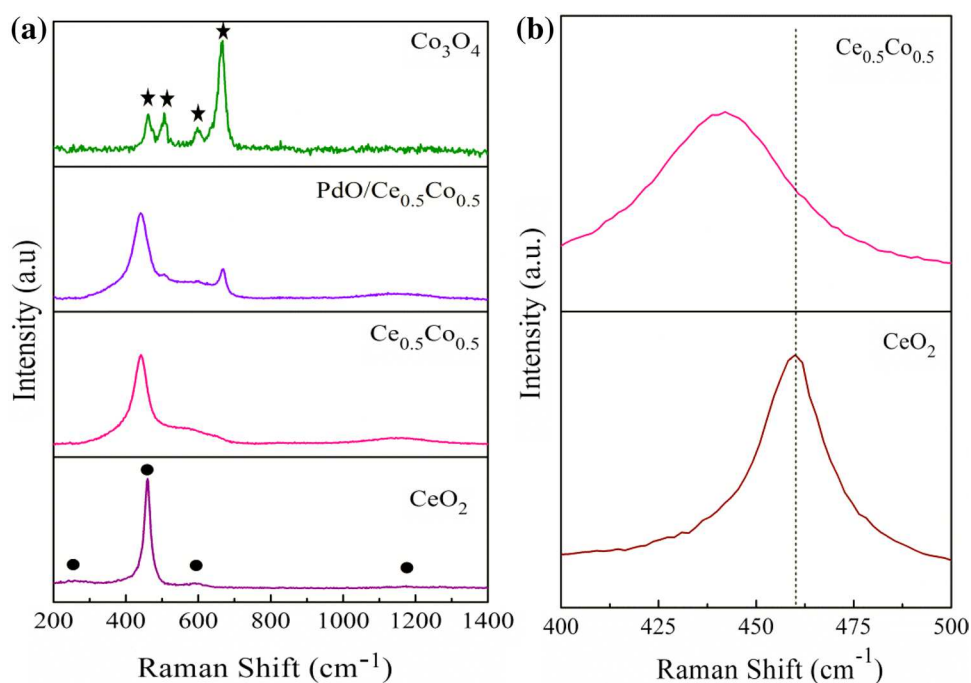
at about 269, 330 and 730 °C respectively and two small humps at low temperature. The first two peaks are ascribed to the two-step reduction of the finely dispersed Co_3O_4 to Co^0 involving CoO intermediate strongly interacted with the supporting CeO_2 [24, 35]. Whereas, a small reduction peak in between these two peaks is due to the interaction between CeO_2 and Co_3O_4. Meanwhile, the reduction of surface Ce^{4+} to Ce^{3+} also occurs in the temperature range and the peak appears as a broad shoulder in the TPR pattern. The wide reduction window at 730 °C is assigned to the conversion of the remaining CeO_2 to Ce_2O_3 i.e. the reduction of bulk oxide species [45, 46]. It is worthy to note that

the Ce(IV) reduction temperature in $Ce_{0.5}Co_{0.5}$ systematically shift towards a lower value compared with the pure CeO_2, strongly suggesting that the interaction of Ce-Co can increase the reducibility of CeO_2 [47]. Previously studies show the introduction of the second metal in ceria resulting in the formation of solid solution and increase of the M-O-Ce bonds, which favors the formation of oxygen vacancy and enhance the mobility of oxygen species from its bulk to the surface dramatically [48, 49].

The addition of PdO to the supporting compound ($Ce_{0.5}Co_{0.5}$) improves the reduction profile significantly. The low temperature reduction doublet moves to lower
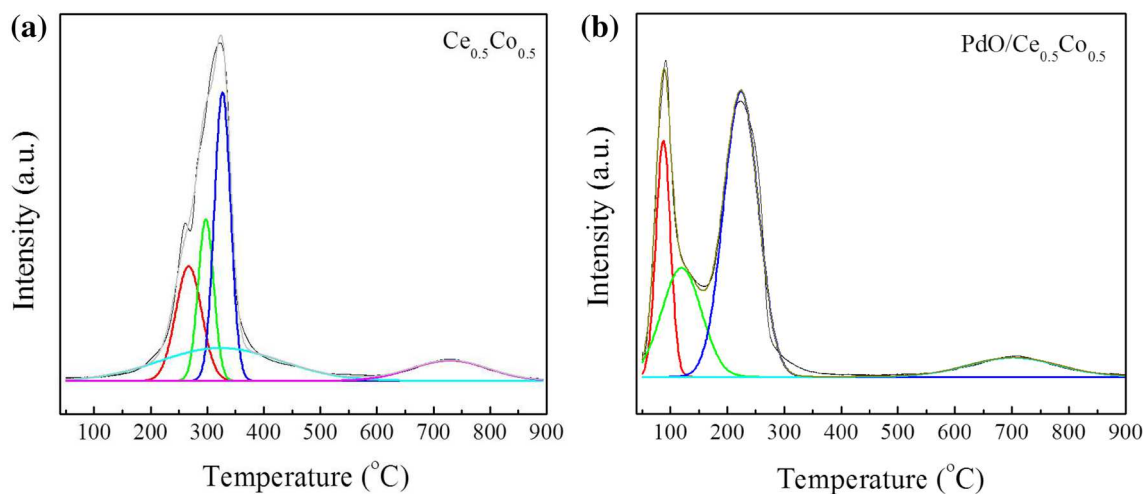
Fig. 5 TPR spectra of $Ce_{0.5}Co_{0.5}$ (**a**) and $Pd/Ce_{0.5}Co_{0.5}$ (**b**)

temperatures, which also witnesses the interaction between the support and the active metal [36]. The peak at around 90 °C is found to be the characteristic reduction peak of Pd^{2+} to Pd^0 [50, 51]. The actual hydrogen amount consumed by PdO (0.32 mmol/g, calculated based on the integrated peak area) is much higher than the theoretical value (0.028 mmol/g), might indicate the reduction of the supporting compound at the temperature and validating the hypothesis of SMSI occurrence. Moreover, the addition of PdO to the catalytic system is thought to enhance the mobility of lattice oxygen as the reduction temperature of bulk oxygen species of CeO_2 phase drop from 730 to 700 °C [13].

3.2 Catalytic Activity

The catalytic performance of $PdO/Ce_{0.5}Co_{0.5}$ and the $Ce_{0.5}Co_{0.5}$ for EA degradation is shown by the conversion vs temperature at 60,000 mL g^{-1} h^{-1} of an inlet EA flow with a concentration of 1500 ppm (Fig. 6). In order to check the effect of PdO addition, the catalytic reaction was comparably carried out by using both the $Ce_{0.5}Co_{0.5}$ and $PdO/Ce_{0.5}Co_{0.5}$ catalysts under similar conditions. The temperature for EA conversion over both catalysts reaching to 10% (T_{10}), 50% (T_{50}) and 90% (T_{90}) of the total conversion is summarized in Table 2.

It is noteworthy that the light-off temperatures for the conversion of EA over $PdO/Ce_{0.5}Co_{0.5}$ (T_{10}/122, T_{50}/155 and T_{90}/182) are significantly lower than those of $Ce_{0.5}Co_{0.5}$ (T_{10}/141, T_{50}/180 and T_{90}/213). Whereas, the complete degradation of EA to CO_2 and H_2O takes place at 198 and 230 °C over the noble metal supported/unsupported catalysts, respectively. Figure 6 shows that the activity of $Ce_{0.5}Co_{0.5}$ is not as good as that of $PdO/Ce_{0.5}Co_{0.5}$. Furthermore, the reaction rate at 140 °C (The EA conversion is lower than 20% at the temperature below 140 °C) over $PdO/Ce_{0.5}Co_{0.5}$ (1.38×10^{-4} mol g_{cat}^{-1} s^{-1}) is two times higher than that of $Ce_{0.5}Co_{0.5}$ (0.75×10^{-4} mol g_{cat}^{-1} s^{-1}) as shown in Table 2.

The above results unambiguously demonstrate the occurrence of SMSI between the support ($Ce_{0.5}Co_{0.5}$) and noble metal (PdO) nanoparticles. Since $Ce_{0.5}Co_{0.5}$ is transition metal, the case might be considered as a general one and extended to other transition metal based supports. We therefore, synthesized the $PdO/Ce_{0.5}Co_{0.5}$ catalyst which is proved to be highly efficient for the catalytic oxidation of EA. The HAADF mapping (Fig. 2c) shows the homogeneous dispersion of the active metal on the support. As confirmed by the catalytic activity results, the support seems to have a significant effect in lowering the degradation temperature of EA.

To evaluate the stability and durability of $PdO/Ce_{0.5}Co_{0.5}$, real-time tests under stream flow have been
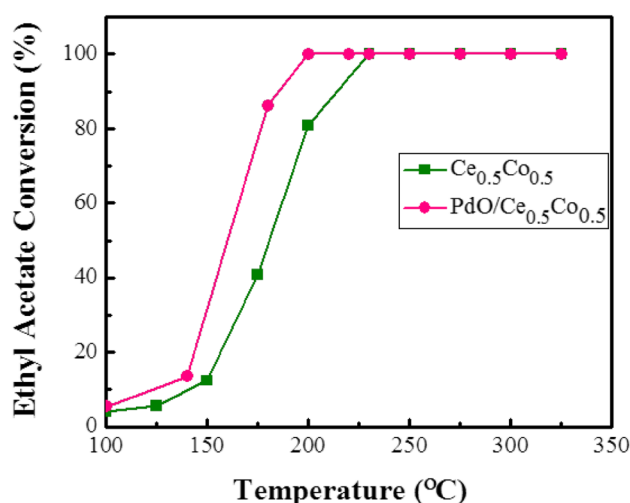
Fig. 6 Ethyl acetate (EA) conversion (%) over $Ce_{0.5}Co_{0.5}$ and $PdO/Ce_{0.5}Co_{0.5}$

Table 2 T_{10}, T_{50} and T_{90} of the catalysts for the catalytic oxidation of ethyl acetate (EA) and the corresponding reaction rate at 140 °C

Samples	EA conversion temperature (°C)			Rate at 140 °C ($\times 10^{-4}$ mol g_{cat}^{-1} s^{-1})
	T_{10}	T_{50}	T_{90}	
$Ce_{0.5}Co_{0.5}$	141	180	213	0.75
$PdO/Ce_{0.5}Co_{0.5}$	122	155	182	1.38

done (Fig. 7). The catalyst was examined at a practical temperature until a complete degradation is achieved (EA flow rate: 60,000 mL g^{-1} h^{-1}, reactant concentration: 1500 ppm and reaction temperature: 230 °C). Figure 7 shows that catalytic activity is stably kept at 100% after a short period of induction for EA degradation over $PdO/Ce_{0.5}Co_{0.5}$ and no obvious catalyst deactivation can be seen after 36 h.

3.3 Drift Analysis

In-situ diffuse reflectance infrared Fourier Transform spectroscopy (DRIFTS) experiments were conducted under the same reaction conditions. Figures 8a, b and 9a, b shows the IR spectra obtained for both the $Ce_{0.5}Co_{0.5}$ and $PdO/Ce_{0.5}Co_{0.5}$ catalyst during the EA oxidation at various temperatures. Over the catalyst of $Ce_{0.5}Co_{0.5}$, the spectrum at room temperature (Fig. 8a) shows an intense band at 1440 cm^{-1} along with a moderate one at 1550 cm^{-1} are attributed to the COO symmetric and asymmetric stretching vibrations respectively. An intense band at 1307 cm^{-1} with a very small hump at 1350 cm^{-1} is denoted to CH_3 symmetric and asymmetric variable angle vibration (COO linked CH_3). Similarly a small low intense peak at 1047 is attributed to the C–O–C symmetric and asymmetric stretching
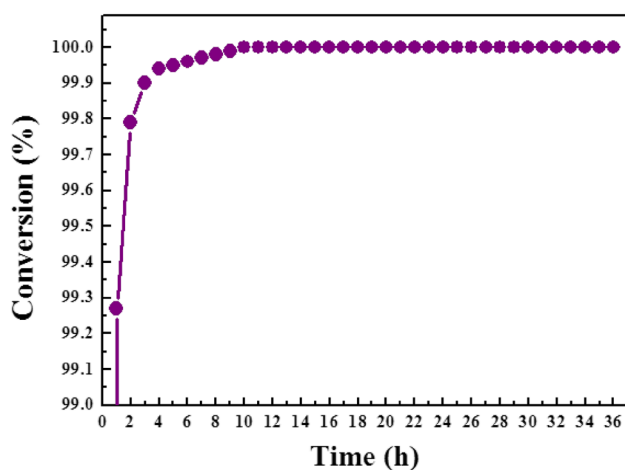
Fig. 7 Catalytic stability test of PdO/Ce$_{0.5}$Co$_{0.5}$ for ethyl acetate (EA) conversion

of acetate [52]. In addition the peaks at 3692, 3300 cm^{-1} and 1642 cm^{-1} are attributed to the hydroxylated species on the surface of catalyst, OH stretching and deviational vibration, respectively. Figure 8b depicts the IR spectra at elevated temperature. With the reaction progress, a new band at 1293 cm^{-1} (CO asymmetric stretching) appears when the temperature rises to 100 °C indicating the formation of acetic acid [53]. In addition, an IR band at 1350 cm^{-1} becomes intense denoting an asymmetric vibration caused by the CH$_3$ molecule linked to COO [54]. Meanwhile, it is worthy to note that the OH band (3300 cm^{-1}) becomes intense with the increase of the temperature along with the appearance of a new band at 1066 cm^{-1} indicating the formation of alcohol [52]. Up to 200 °C, no any new peaks appear except the intensity of OH band increases due to the increased concentration of alcohol. Another evidence on the formation of alcohol is the change of the band at 1647 cm^{-1}, the out-of-plane deviational vibration of OH
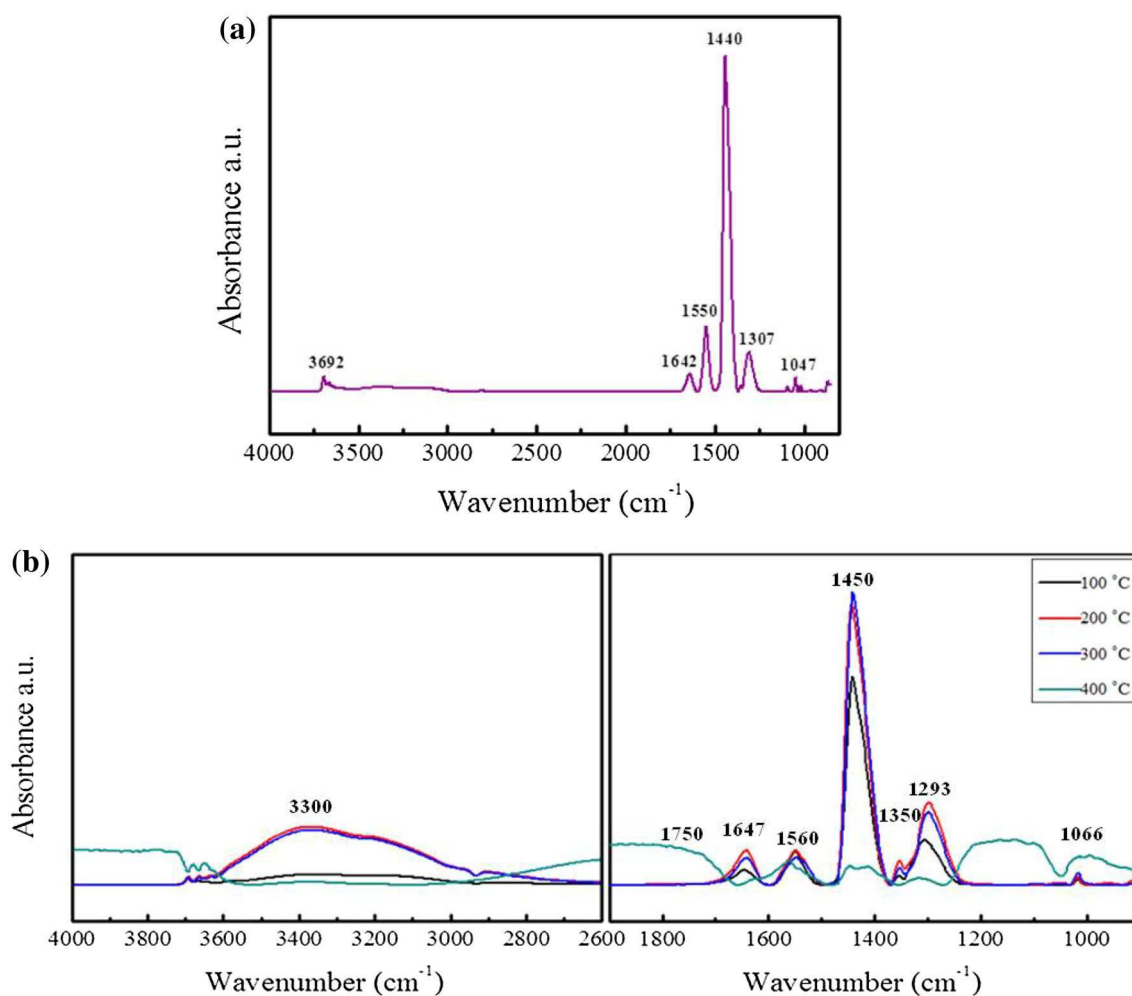
Fig. 8 In-situ FTIR spectra of Ce$_{0.5}$Co$_{0.5}$ at room temperature (**a**) and at elevated temperature (**b**)

group since no liquid species are stable on this temperature. The peaks at 300 °C are almost similar to those at 200 °C. However, the FTIR bands changes dramatically at 400 °C. At this temperature, the FTIR spectra for O–C=O stretching at 1450, 1560 and 1320 cm^{-1} and a broad shoulder around 1750 cm^{-1} C=O stretching appear [52, 53]. It is worthy to note that the peaks of alcohols disappear when those of acetate species appear indicating that alcohol is no longer an intermediate product at the temperature where the EA is totally converted into acetic acid and further decomposed into the final product, CO_2 and H_2O.

Over Pd/Ce$_{0.5}$Co$_{0.5}$ (Fig. 9a, b), the in-situ FTIR band at room temperature and 100 °C is quite similar to that of the Ce$_{0.5}$Co$_{0.5}$ compound and the only difference is the intensity of the OH peak, which indicates the surface absorbed EA is easier to be oxidized by active oxygen species at low temperature. At 300 °C the FTIR bands over PdO/Ce$_{0.5}$Co$_{0.5}$ catalyst are similar to those reacted at 400 °C over Ce$_{0.5}$Co$_{0.5}$ compound, confirms the degradation reaction can occur at lower temperature caused by the strong SMSI.

3.4 Ethyl Acetate Degradation Mechanism

In the light of in-situ FTIR the oxidative degradation mechanism of EA is proposed (Fig. 10). When the molecules of EA contact with the catalyst, they are adsorbed on the surface and activated due to its electron-deficient acidity nature (Fig. S8), the detailed surface acidic and basic analysis is given in SI (Fig. S6, S7 and Table S1). The C-O bond of the activated EA molecules is cleaved by the assistance of the hydroxyl species on the surface. After that, acetic acid and ethanol are produced [55] as shown in Fig. 10. The energetic gaseous oxygen species are absorbed
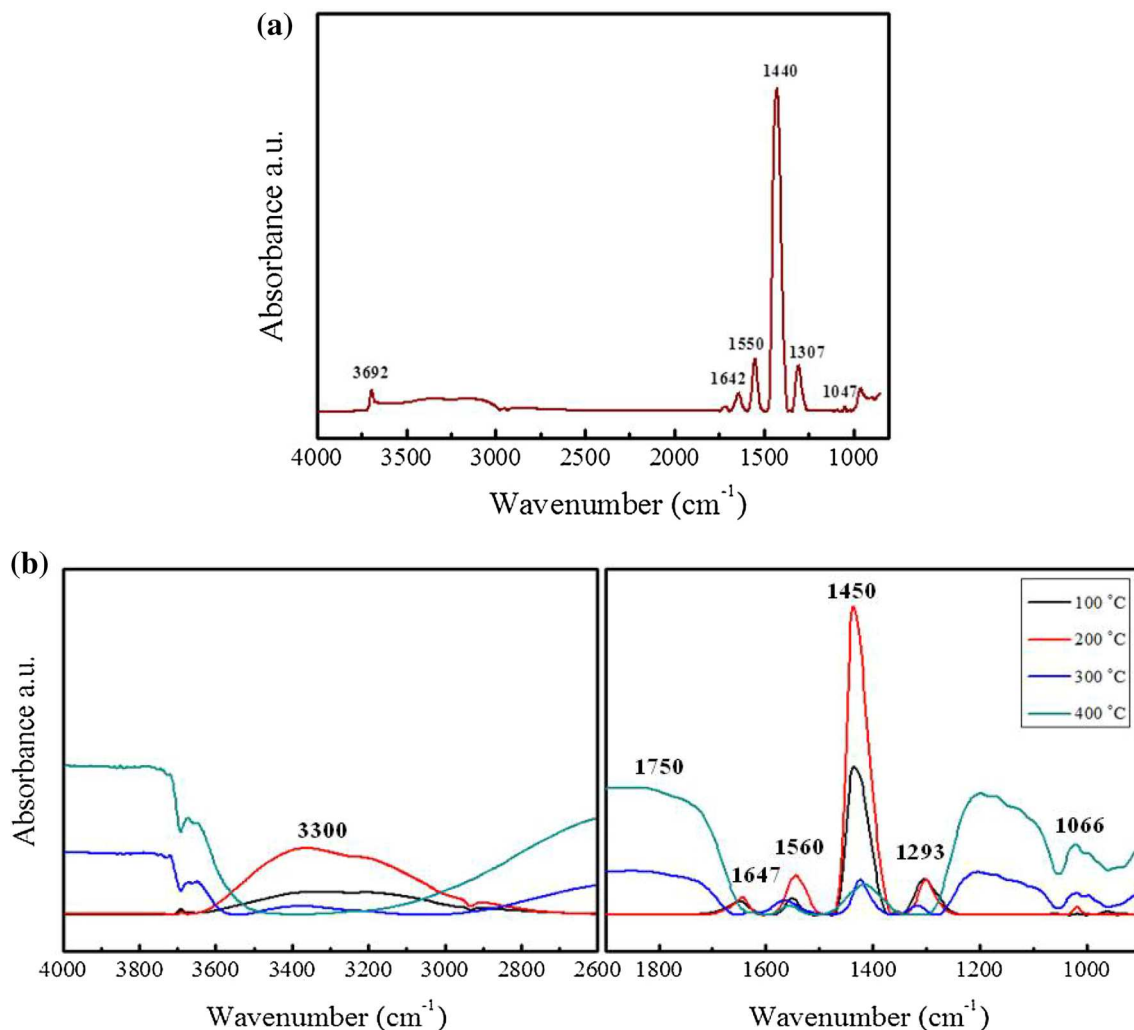
Fig. 9 In-situ FTIR spectra of PdO/Ce$_{0.5}$Co$_{0.5}$ at room temperature (**a**) and elevated temperature (**b**)

Fig. 10 Schematic reaction mechanism for ethyl acetate (EA) degradation
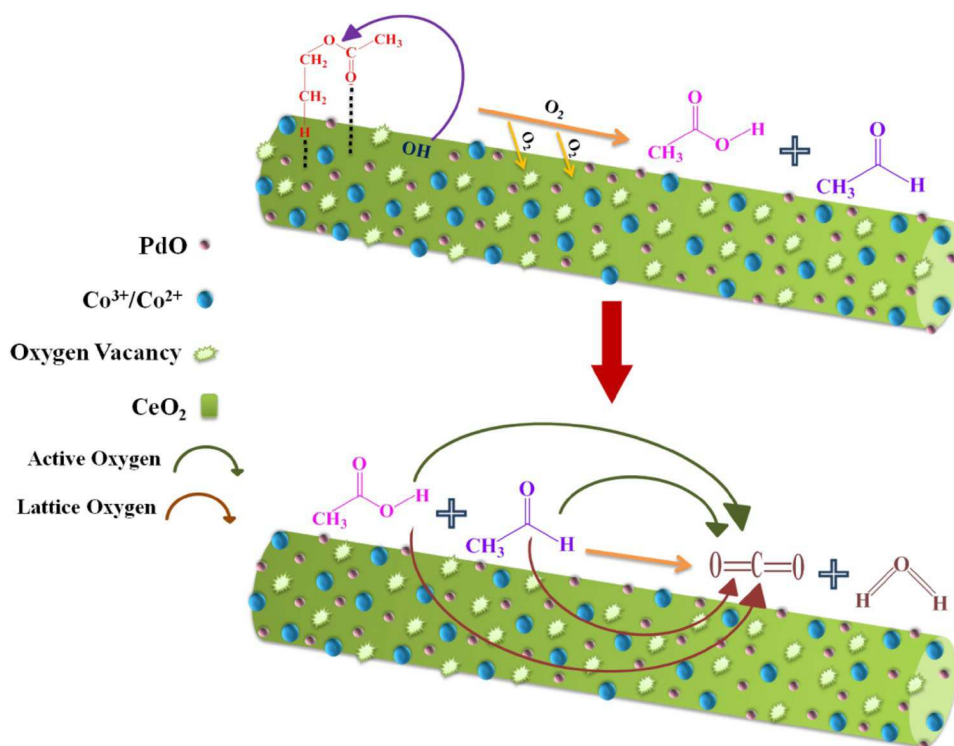
on the oxygen vacancies on the catalyst surface to form O_2^- which is able to oxidize acetic acid molecules to final product, where the cleaved species, i.e. acetic acid and ethanol are oxidized by the lattice oxygen following the Mars-van Kerevlen mechanism. With the progress of the reaction, acetic acid and ethanol are continuously oxidized to CO_2, H_2O by the oxygen species diffused from feed stream to the surface of a catalyst and then from the bulk (lattice) to the surface via the so-called vacancy hopping mechanism [56]. It is worthy to note that no other by-products appear in both the catalytic systems, either supported PdO or support as seen by the DRIFT spectra confirming that the pathway of the EA degradation is similar over both catalysts. The role of PdO here is thought to enhance the activation of oxygen species in two ways, firstly, it increases the dissociation rate of the oxygen from the feed flow [33] and secondly, it increases the mobility of the oxygen species on the surface of the catalyst [13]. Moreover, no any aldehydes bands are observed in in-situ FTIR analysis, indicating that a green degradation of EA is achieved by these catalysts under the experiment conditions without the formation of any harmful intermediates.

To summarize, it is speculated that the performance of the Ce/Co-supported PdO catalyst (Pd/Ce$_{0.5}$Co$_{0.5}$) is better than the support (Ce$_{0.5}$Co$_{0.5}$) for the degradation of EA. It is not surprising taking into account the crucial role of PdO to enhance the activation of oxygen species [40], ultimately increasing the rate of reaction. The even dispersion of the PdO throughout the whole body of the support and

the SMSI is of primary importance for the catalytic activity. Furthermore the electron deficient acidic sites on the support favor the adsorption and cleavage of the reactant molecule (EA) to ethanol and acetic acid and further oxidized to final products following the Mars-van Kerevlen mechanism.

4 Conclusion

Ce/Co-supported PdO catalyst (PdO/Ce$_{0.5}$Co$_{0.5}$) have been synthesized and used to degrade EA at reduced temperature under concentrated feed stream. The effect of PdO addition and its interaction with the support has been investigated by structural, textural, spectroscopic techniques and redox properties on a model catalytic system. The catalytic performance of the catalysts confirm that Ce/Co-supported PdO catalyst can further lowers the EA degradation temperature (T$_{90}$) from 213 to 182 °C under concentrated feed stream as compared with the support. Furthermore, in-situ DRIFT analysis is used to interpret the EA degradation mechanism over different catalytic system and the results show that no other harmful intermediate products, such as aldehydes other than alcohols and acetates is produced suggesting this a green approach.

References

1. Unger K (2006) Science 312:823
2. Matheson RR (2002) Science 297:976–979
3. Hutchings GH, Heneghan CS, Hudson LD, Taylor SH (1996) Nature 384:341–343
4. Rappaport SM, Kupper LL (2004) J Expo Anal Env Epid 14:92–107
5. Chen X, Carabineiro SAC, Bastos SST, Tavares PB, Orfao JJM, Pereira MFR, Figueiredo JL (2013) J Environ Chem Eng 1:795–804
6. Dai Q, Huang H, Zhu Y, Deng W, Bai S, Wang X, Lu G (2012) Appl Catal B Environ 117–118:360368
7. Yang Y, Xu X, Sun K (2007) J Hazard Mater B 139:140–145
8. Zhang F, Pan L, Li T, Diulus JT, Asthagiri A, Weaver JF (2014) J Phys Chem C 118:28661–28674
9. Chin YH, Iglesia E (2011) J Phys Chem C 115:17845–17855
10. Kinnunen NM, Hirvi JT, Suvanto M, Pakkanen TA (2011) J Phys Chem C 115:19197–19202
11. Cubeiro ML, Fierro JLG (1998) Appl Catal A Gen 168:307–322
12. Jin MS, Park JN, Shon JK, Kim JH, Li ZH, Park YK, Kim JM (2012) Catal Today 185:183–190
13. Wang W, Yuan F, Niu X, Zhu Y (2016) Scientific Reports 6:19511
14. Zhang J, Li Y, Chen M, Wang L, Zhang C, He H (2015) Scientific Reports 5:12950
15. Zhang T, Li W, Croue JP (2011) Environ Sci Technol 45:9339–9346
16. Atkinson A, Barnett S, Gorte RJ, Irvine JTS, Mcevoy AJ, Mogensen M, Singhal SC, Vohs J (2004) Nat Mater 3:17–27
17. Murugan Ramaswamy AV (2007) J Am Chem Soc 129:30623063
18. Cwele T, Mahadevaiah N, Singh S, Friedrich HB (2016) Appl Catal B Environ 182:1–14
19. Li G, Li L, Jiang D (2015) J Phys Chem C 119:12502–12507
20. Liotta LF, Ousmane M, Carlo GD, Pantaleo G, Deganello G, Marci G, Retailleau L, Fendler AG (2008) Appl Catal A Gen 347:81–88
21. Akram S, Wang Z, Chen L, Wang Q, Shen GL, Han N, Chen Y, Ge G (2016) Catal Comm 73:123–127
22. Trovarelli A (2002) Catalysis by Ceria and related materials. London, Imperial college press
23. Wang Z, Yang M, Shen GL, Liu HD, Chen YF, Wang Q (2014) J Nanopart Res 16:2367
24. Wang Z, Shen GL, Liu HD, Wang Q, Chen YF (2013) Appl Catal B Environ 138:253–259
25. Yang P, Yang S, Shi Z, Meng Z, Zhou R (2015) Appl Catal B Environ 162:227–235
26. Wyrwalski F, Giraudon JM, Lamonier JF (2010) Catal Lett 137:141–149
27. Huang H, Dai QG, Wang XY (2014) Appl Catal B Environ 158–159:96–105
28. Tan H, Wang J, Yu S, Zhou K (2015) Envir Sci Technol 49:8675–8682
29. Fau P, Schierbaum KD (1994) Surf Sci 321:71–80
30. Xiao WD, Guo QL, Wang EG (2003) Chem Phys Lett 368:527–531
31. Lenormand F, Hilaire L, Kili K, Krill G, Maire G (1988) J Phys Chem 92:2561–2568
32. He C, Yu Y, Yue L, Li J, Shen Q, Yu W, Chen J, Hao Z (2014) Appl Catal B Environ 147:156–166
33. Luo JY, Meng M, Li X, Li XG, Zha YQ, Hu TD, Xie YN, Zhang J (2008) J Catal 254:310–324.
34. Ichimura K, Inoue Y, Yasumori I (1980) Bull Chem Soc Jpn 53:3044
35. Tang W, Wu X, Li D, Wang Z, Liu H, Chen Y (2014) J Mater Chem A 2:2544
36. Narayanappa M, Dasireddy VDBC, Friedrich H (2012) Appl Catal A Gen 447–448:135–143
37. Naresh D, Kumar VP, Harisekhar M, Nagaraju N, Putrakumar B, Cherry KVR (2014) Appl Surf Sci 314:199–207
38. Harikrishna Y, Kumar VP, Ramu K, Cherry KVR, Rao VV (2015) Appl Petrochem Res 5:71–80
39. Otto K, Haack LP, Devries JE (1992) Appl Catal B Environ 1:1–12
40. Rashad M, Rusing M, Berth G, lischka K, Pawlis A (2013) J Nanomaterial 2013:714853.
41. Ercolino G, Grzybek G, Stelmachowski P, Specchia S, Kotarba A, Specchia V (2015) Catal Today 275:66–71
42. Thammachart M, Meeyoo V, Risksomboon T, Osuwan S (2001) Catal Today 68:53–61
43. Chang S, Li M, Hua Q, Zhang L, Ma Y, Ye B, Huang W (2012) J Catal 293:195–204
44. Wang Z, Wang Q, Liao Y, Shen GL, Gong X, Han N, Liu H, Chen Y (2011) Chem Phys Chem 12:2763–2770
45. Dai QG, Huang H, Zhou Y, Deng W, Bai SX, Wang XY, Lu GZ (2012) Appl Catal B Environ 117–118:360–368
46. Rivas BD, Fonseca RL, Ortiz MAG, Ortiz JIG (2011) Appl Catal B Environ 101:317–325
47. Xue L, Xue L, Zhang C, He H, Teraoka Y (2007) Appl Catal B Environ 75:167–174
48. Cen W, Liu Y, Wu Z, Wang H, Weng X (2012) Phy Chem Chem Phy 14:5769–5777
49. Zhang P, Lu H, Zou Y, Zhang L, Wu Z, Yang S, Shi H, Zhu Q, Chen Y, Dai S (2015) Nat Commun 6:8446
50. Tang XF, Chen JL, Li YG, Li Y, Xu YD, Shen WJ (2006) J Chem Eng 118:119–125
51. Priolkar KR, Bera P, Sarode PR, Hegde MS, Emura S, Kumashiro R, Lalla NP (2002) Chem Mater 14:2120–2128
52. Phung TK, Casaza AA, Aliakbarian B, Finocchio E, Perego P, Busca (2013) G Chem Eng J 215–216:838–848
53. Hauchecorne B, Terrens D, Verbruggen S, Martens JA, Langenhove HV, Demeestere K, Lenaerts S (2011) Appl Catal B Environ 106:630–638
54. Phung TK, Carnasciali MM, Finocchio E, Busca G (2014) Appl Catal A Gen 470:72–80
55. Larsson PO, Andersson A (2000) Appl Catal B Environ 24:175–192
56. Catlolw CRA (1990) J Chem Soc Faraday Trans 86:1167–1176